Journal of Alloys and Compounds 747 (2018) 1008–1017

Contents lists available at ScienceDirect

Journal of Alloys and Compounds

journal homepage: http://www.elsevier.com/locate/jalcom

Low temperature ferromagnetism in Rh-rich Fe-Rh granular nanowires

J.S. Riva [a, b], G. Pozo-López [a, b, c], A.M. Condó [a, d], L.M. Fabietti [a, b, c], S.E. Urreta [b, *]

[a] Consejo Nacional de Investigaciones Científicas y Técnicas (CONICET), Argentina
[b] Universidad Nacional de Córdoba. Facultad de Matemática, Astronomía, Física y Computación, Ciudad Universitaria, 5000, Córdoba, Argentina
[c] Instituto de Física Enrique Gaviola – CONICET, Córdoba, Argentina
[d] Centro Atómico Bariloche, Comisión Nacional de Energía Atómica – Instituto Balseiro, Universidad Nacional de Cuyo, Av. Bustillo 9500, 8400, San Carlos de Bariloche, Argentina

ARTICLE INFO

Article history:
Received 13 January 2018
Received in revised form
3 March 2018
Accepted 8 March 2018
Available online 9 March 2018

Keywords:
Fe-Rh polycrystalline nanowires
AC electrodeposition
Low temperature ferromagnetism
Spin glass boundary phase
Magnetization mechanism

ABSTRACT

Noble/transition bimetallic nanowires of nominal composition Fe_xRh_{100-x} (x = 15, 25, 54) are AC electrodeposited into 20 nm diameter hexagonally self-assembled nanopores of anodic alumina membranes. Nanowires about 18 nm in diameter and 1 μm long are polycrystalline and, depending on composition, different crystalline phases are obtained. Iron-rich (x = 54) wires are biphasic, composed by large α-Fe grains (>100 nm in length) and clusters of small (3 nm in average) grains of *fcc* γ-Rh(Fe) phase, with composition near (30 ± 5) at% Fe. Rh-rich (x = 15, 25) nanowires are formed by very small grains of γ-Rh(Fe) phase. Grain size depends on Rh content: grains in wires with x = 15 are the smallest with a mean size of (2.1 ± 0.9) nm. The low temperature magnetic properties of these small grained nanowires exhibit new features: they are all ferromagnetic at 5 K while, at room temperature wires with 54 at.% Fe and 25 at.% Fe are ferromagnetic and those with 15 at.% Fe are weakly superparamagnetic. These behaviors are consistent with non-compensated and very small ferrimagnetic grains surrounded by a grain boundary disordered spin-glass-like phase that freezes below 40 K. This frozen intergranular phase favors a strong exchange coupling between the ferrimagnetic grains, which undergo a cooperative, ferromagnetic-like behavior under an external magnetic field. Above 40 K nanowires with 54 at.% Fe are ferromagnetic and those containing 25 at.% Fe exhibit a ferromagnetic-like behavior arising from blocked antiferromagnetic grains. Nanowires 15 at.% Fe are weakly superparamagnetic above 40 K. Arrays containing 54 at.% Fe and 25 at.% Fe exhibit a polarization reversal mechanism involving localized nucleation and further expansion of inverse domains; this thermally activated, magnetic field assisted mechanism exhibits an apparent activation energy between 229 kJ/mol (2.3 eV) and 298 kJ/mol (3.1 eV) for nanowires 25 at.% Fe and 54 at.% Fe, respectively.

1. Introduction

Nanostructures containing noble and magnetic metals may be tailored to improve their performance in catalysis and sensing, by controlling their size, shape, composition and surface properties [1–4]. Bimetallic nanowires with high aspect ratios are also found to be suitable for applications in sensors and/or catalysts and electro-catalysts.

Microstructure requirements for these applications include polycrystalline multiphase wires, with small grain size as they provide irregular surfaces with areas chemically and crystallographically different, with also distinct properties. In this sense Lee et al. [5] showed that both, the H_2 detection limit and the response time, are smaller in nanowires with a rough surface, approximately 20 times shorter than that of the smooth, as-grown one.

Near the equiatomic composition, FeRh alloys undergo a magnetic and structural transformation [6] from an antiferromagnetic to a ferromagnetic phase on heating above about 400 K [7]. This transformation makes these alloys active materials in heat pumps and refrigerators [8,9]. Moreover, nanostructures with Rh-rich compositions are important catalysts in many organic reactions

* Corresponding author. Universidad Nacional de Córdoba. Facultad de Matemática, Astronomía, Física y Computación. Ciudad Universitaria, 5000, Córdoba, Argentina
E-mail address: urreta@famaf.unc.edu.ar (S.E. Urreta).

https://doi.org/10.1016/j.jallcom.2018.03.091
0925-8388/

[10].

In addition to the magnetic functionality, magnetic catalysts have the advantage that they may be easily recovered and reused many times providing a practical technique for recycling the magnetized nanostructured catalysts [11].

In recent research works we reported the first results in Fe-rich Fe-Rh nanowires [12,13]. However, no data are available at present concerning Fe-Rh nanowires containing 50–85 at.% Rh.

In this article, Fe-Rh nanowires with different nominal compositions are successfully synthesized by AC electrodeposition into alumina hard templates. For the first time, Rh-rich nanowires are investigated. The complex "as synthesized" microstructures are characterized in detail and the magnetic hysteresis properties, such as coercivity and relative remanence, are determined in the temperature range between 5 K and 300 K. The magnetization mechanism in these granular, multiphase nanowires is investigated, and the activation energy barrier for inverse domain nucleation as a function of the observed microstructure is roughly estimated.

2. Experimental details

Anodized aluminum oxide (AAO) membranes, used as hard templates, are prepared by the well-known two-step anodization method [14], starting from a high-purity aluminum foil (99.995%, Alfa AEsar). The aluminum foils were first degreased with acetone, electro-polished in a H_2SO_4 + H_3PO_4 + H_2O 2:2:1 solution, and finally etched with NaOH to remove aluminum oxide from the surface. The foil was anodized under a constant voltage of 20 V in 0.3 M $H_2C_2O_4$ for 4 h at 276 K to form a layer of porous alumina. After the first anodizing step, the aluminum oxide film was dissolved in 0.20 M Cr_2O_3 and 0.40 M H_3PO_4 at 333 K for 1 h, to remove the oxide layer. The second anodizing step was carried out under the same conditions as the first one, for another 2 h. In these conditions, arrays of ordered pores, 20 nm in diameter and about 3 μm in length, were obtained (Fig. 1a). The membrane porosity P was estimated as $P = (\pi/2\sqrt{3})\ (D/D_{int})^2 = 0.10 \pm 0.01$ [15], with $D = (20 \pm 2)$ nm the pore diameter and $D_{int} = (60 \pm 4)$ nm the mean centre-to-centre interpore distance in the array.

Fe-Rh nanowires were prepared by AC electrodeposition from an aqueous electrolytic bath containing different proportions of $FeSO_4 \cdot 7H_2O$ and $RhCl_3$, 0.75 g/L ascorbic acid (to avoid iron oxidation), and 30 g/L H_3BO_3, maintaining the pH value at 4.0. Electrodeposition was carried out at room temperature with an AC voltage between 15 and 20 V_{rms} and 60–100 Hz during a few minutes. A two electrode electrochemical cell was used, where the aluminum still attached to the AAO template served as a working electrode and a graphite rod as an auxiliary one; oxygen was purged from the solutions by nitrogen bubbling before the experiments.

X-ray diffraction (XRD) was used to identify the phases in the nanowires; XRD profiles were recorded in a PANalytical Empyrean diffractometer, using Cu Kα radiation (λ = 1.5418 Å), in the 2θ range from 30° to 90°.

Samples for XRD measurements were prepared by dissolving the remaining Al substrate in a $CuSO_4$ and HCl solution to eliminate intense Al X-ray peaks; samples for SEM observations were further immersed in a 1.0 M NaOH solution to dissolve the AAO template and separate the nanowires. After sonication and rinsing in ultrapure water, dispersed nanowires were obtained, as illustrated in Fig. 1b to 1 d.

The nanowire morphology was investigated in a scanning electron microscope FE-SEM Zeiss; the mean array composition was determined by energy-dispersive X-ray spectroscopy (EDS) in the SEM, after three determinations involving large areas in each array. Thus, samples are named by the iron content as Fe54 ($Fe_{54}Rh_{46}$), Fe25 ($Fe_{25}Rh_{75}$) and Fe15 ($Fe_{15}Rh_{85}$). These mean compositions are actually nominal, because some nanowires are multiphase, as will be seen below.

The individual wire nanostructure and composition were investigated by transmission electron microscopy (TEM) in a Philips CM200 UT and a FEI TECNAI F20 G2 microscopes, operating at

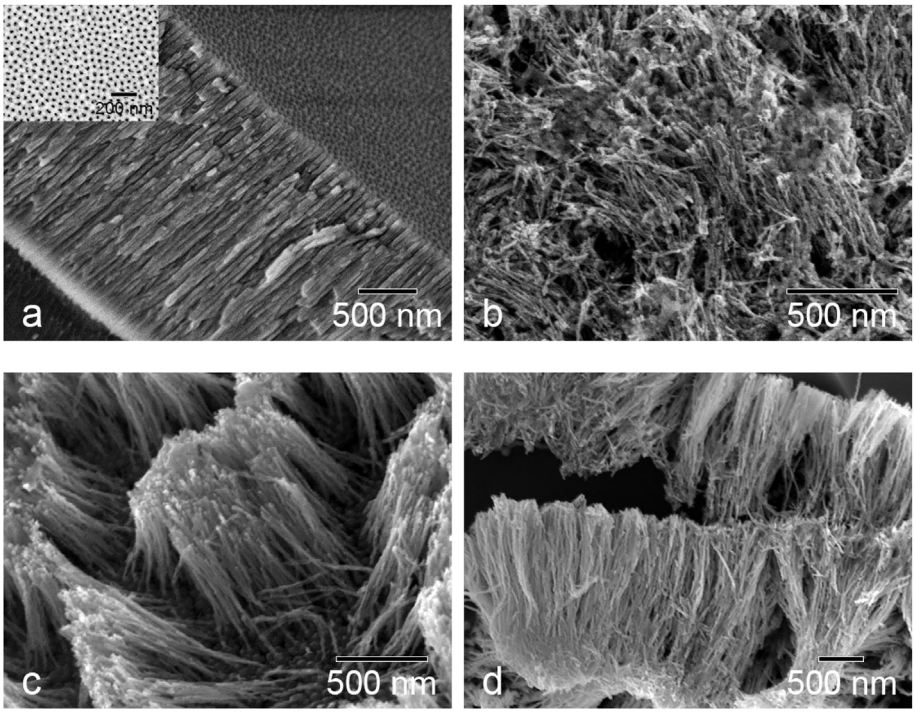

Fig. 1. SEM micrographs showing: (a) a side view of an alumina template of 20 nm pore diameter; *inset*: top view. Nanowires Fe15 (b), Fe25 (c) and Fe54 (d) are observed after the removal of the aluminum support and the partial dissolution of the alumina template (see text for samples' nomenclature).

200 kV. The mean composition of each phase was determined with an EDS nanoprobe in the TEM. Samples for TEM observations were prepared by dispersing the liberated nanowires in ethanol and further depositing a drop of this emulsion on a holey carbon-coated copper grid.

Magnetic properties of Fe-Rh nanowires were measured in a SQUID magnetometer at different temperatures up to a maximum field of 1.5 T. The external field was applied parallel (PA) and perpendicular (PE) to the nanowire long axis. Samples had areas of (6×2) mm^2. The total magnetic moment of the assembly has contributions from the Al support (paramagnetic), the alumina template (diamagnetic) and the metallic wires filling the pores (ferromagnetic), so the ferromagnetic component must be estimated after subtracting the other contributions.

When necessary, the hysteresis loops were analyzed considering a linear contribution superimposed to a ferromagnetic one given by Ref. [16]:

$$J_{FM} = \frac{2J_S}{\pi} \arctan\left[\frac{(H \pm H_C)}{H_C} \tan\left(\frac{\pi J_R}{2J_S}\right)\right] \quad (1)$$

Here J_S, $\mu_0 H_C$ and J_R are the saturation polarization, the coercive field and the remanent polarization, respectively, associated to the ferromagnetic contribution and $\mu_0 H$ is the applied field.

3. Results and discussion

3.1. Morphology and structure

Fig. 1 a shows a SEM image of the cross section of a ~3 μm thick alumina membrane (an upper view is provided in the inset). Fig. 1b to 1 d illustrate the nanowire morphology after removing the aluminum support and partially dissolving the alumina template in 0.1 M NaOH. Nanowires of about 20 nm in diameter and (1.1 ± 0.4) μm in length are observed.

X-ray diffractograms of the as-prepared Fe-Rh nanowires embedded into the AAO template, are shown in Fig. 2. The aluminum substrate was partially removed from the backside of the samples, since the (200) diffraction line from Al is still visible. Additionally, (111) and (200) diffraction lines from Cu are observed, arising from residual copper crystals from the saturated copper solution in HCl used to remove the Al support.

In addition to these lines, XRD profiles of Fe-Rh samples exhibit small and broad peaks, probably due to small grain size and crystalline defects. The presence of the α-Fe(Rh) *bcc* phase (PDF # 00-006-0696) cannot be ruled out, since its most intense diffraction line coincides with the position of the residual aluminum line. For the three samples investigated, diffractograms reveal broad and small humps at 2θ ~41°, which are indexed as the (111) line of the γ-Rh(Fe) *fcc* phase (PDF # 00-005-0685), suggesting the presence of this phase with a very small grain size. This *fcc* phase is further confirmed by TEM results, but no lattice parameter could be accurately estimated. Different values have been reported; C. C. Chao et al. measured $a = 3.778$ Å for Fe25 and $a = 3.779$ Å for Fe15 [17], in single-phase, metastable *fcc* Fe-Rh alloys obtained by rapid quenching from the liquid. L. J. Swartzendruber [18] reports similar values ($a = 3.776$ Å for Fe25 and $a = 3.788$ Å for Fe15), both measured at room temperature.

The nanostructure and composition of the individual Fe-Rh wires were further investigated by TEM. Nanowires with the higher iron content (Fe54) exhibit a branched shape, with a quite irregular surface and mean length < 1.5 μm, as can be seen in the bright field (BF) TEM micrograph presented in Fig. 3 a. Selected area electron diffraction (SAED) patterns and EDS spectra indicate that the Fe54 nanowires are biphasic, consisting of segments of *bcc* α-Fe

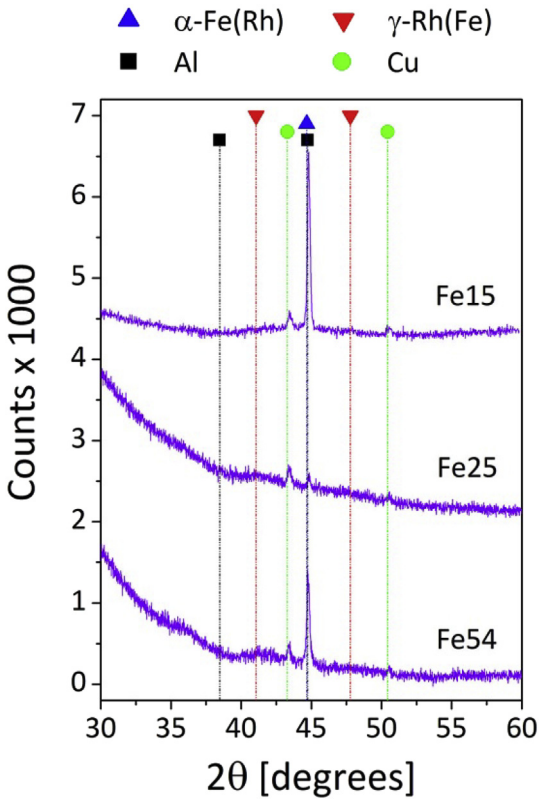

Fig. 2. XRD patterns of Fe_xRh_{100-x} nanowire arrays embedded into the pores of the alumina templates, after dissolving in a large extent the aluminum substrate. Diffraction lines from α-Fe(Rh) and γ-Rh(Fe) phases are indicated, together with the corresponding ones for residual copper crystals and aluminum substrate.

phase and between them another segments of a fine grained *fcc* γ-Rh(Fe) phase. The individual spots and indices shown in the inset of Fig. 3 a correspond to the *bcc* α-Fe phase (indicated with red rings), and the diffraction rings, marked with yellow segments, to the *fcc* γ-Rh(Fe) phase (for the indices corresponding to the *fcc* structure please see Fig. 4a). Ferromagnetic α-Fe segments are composed by quite large grains with longitudinal sizes >100 nm and lateral sizes similar to the wire diameter (mean diameter of (25 ± 6) nm). As already observed in Fe and $Fe_{90}Rh_{10}$ nanowires [12], the α-Fe segments are coated by a thin layer of magnetite, (4 ± 2) nm thick, formed by very small grains, (2 ± 1) nm grain size (Fig. 3b). The additional diffraction rings observed in the SAED pattern of Fig. 3 a, marked with white arrows, are assigned to the magnetite phase (Fe_3O_4). This superficial oxide forms during the subsequent baths applied during sample preparation for TEM. In Fig. 3b, a HRTEM image of a Fe nanowire, with a magnetite layer, beside a Rh-rich nanowire segment can be observed. This image corresponds to the zone marked with a red rectangle in the BF micrograph of the inset, showing the two kinds of segments found in sample Fe54. The FFT (Fast Fourier Transform) of the complete image, displayed in the other inset, shows two rings of spots corresponding to the 111 and 200 *fcc* reflections of the γ-Rh(Fe) nanowire segment, indicated with red circles, and additional spots (Fe and M) corresponding to the α-Fe nanowire and its layer of magnetite, respectively. The bright field image (Fig. 3c) and corresponding dark field image (Fig. 3d) of a group of nanowires illustrate the different morphologies of the two segments. The α-Fe segment is observed as a single bright grain in the DF image, while the γ-Rh(Fe) segment shows much more smaller grains. Fig. 3e and 3 f depict the wire diameter histograms of each kind of segment; note that the mean

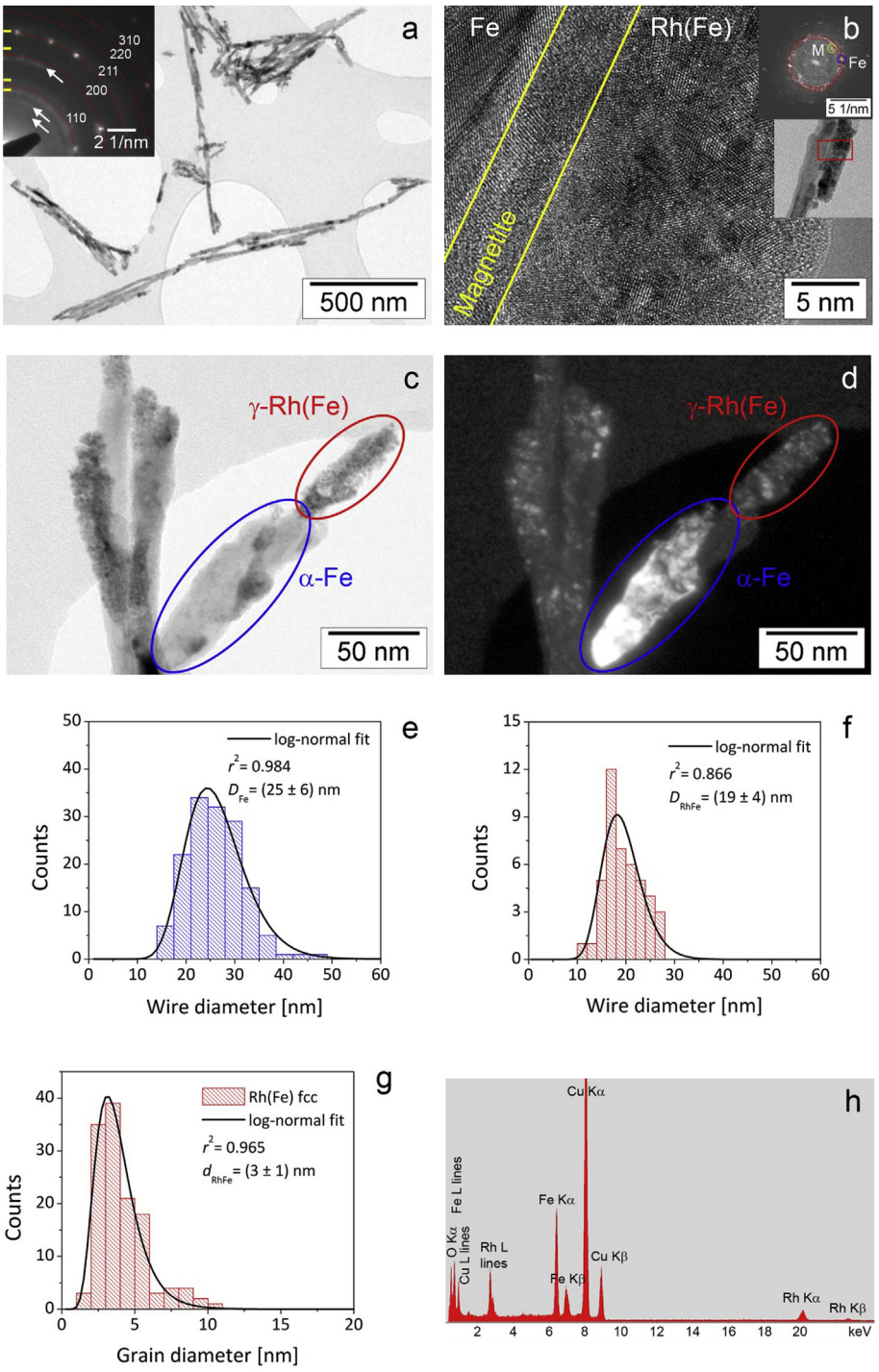

Fig. 3. Fe54 nanowires. (a) Bright field (BF) TEM micrograph and corresponding SAED pattern (included as inset). See text for details. (b) HRTEM image of the zone marked with a red rectangle in the BF micrograph of the inset, showing a detail of the two kinds of segments found in sample Fe54. The FFT of the complete image shows two rings corresponding to the 111 and 200 *fcc* reflections of the γ-Rh(Fe) nanowire and additional spots corresponding to the α-Fe nanowire (Fe) and its layer of magnetite (M). (c) Bright field image and (d) corresponding dark field image of a group of segments with both 111 *fcc* and 110 *bcc* reflections. (e) Wire diameter histograms for α-Fe and (f) γ-Rh(Fe) segments, and it corresponding log-normal fits, resulting from TEM data. (g) γ-Rh(Fe) phase grain size histogram and its corresponding log-normal fit. (h) EDS spectrum of the Fe54 nanowires. Cu lines arise from the TEM grid. (For interpretation of the references to colour in this figure legend, the reader is referred to the Web version of this article.)

wire diameter for the α-Fe phase, excluding the oxide film, results in an average of 17 nm, which is indistinguishable with the one obtained for the γ-Rh(Fe) segments: (19 ± 4) nm. The grain size distribution of the *fcc* γ-Rh(Fe) phase was fitted by a lognormal function leading to a mean value of about (3 ± 1) nm, see Fig. 3 g. The EDS spectrum in Fig. 3 h corresponds to the Fe54 nanowires, including both kinds of segments. Analyzing only the Rh-rich phase, a composition of (30 ± 5) at.% Fe - (70 ± 5) at.% Rh is obtained.

Nanowires with iron contents below 30 at.% are single-phase. In samples Fe25 and Fe15 the only phase detected is the *fcc* γ-Rh(Fe) phase, which is reported to be paramagnetic [18]. Fig. 4 shows

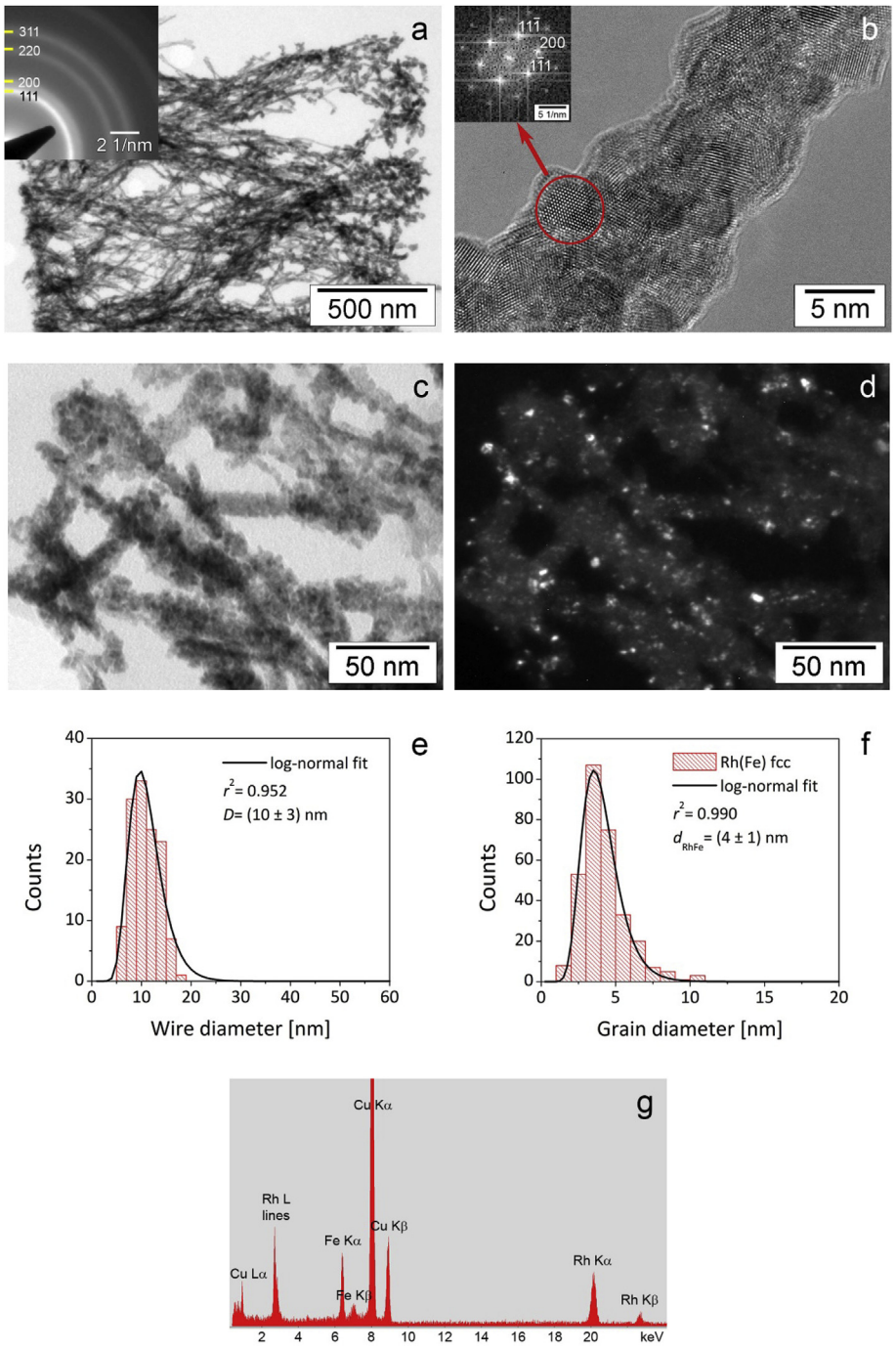

Fig. 4. Fe25 nanowires. (a) TEM overview and corresponding SAED pattern. Indexed electron diffraction rings (indicated with yellow segments) correspond to the γ-Rh(Fe) *fcc* phase. (b) HRTEM image of a Fe25 nanowire. The FFT of one grain, corresponding to the [011] γ-Rh(Fe) zone axis, is shown in the inset. (c) Bright field micrograph and (d) corresponding dark field image with 111 *fcc* reflection, showing small γ-Rh(Fe) grains. (e) Wire diameter and (f) grain size histograms and corresponding log-normal fits, resulting from TEM data. (g) EDS spectrum of the γ-Rh(Fe) phase nanowires. Cu lines arise from the TEM grid. (For interpretation of the references to colour in this figure legend, the reader is referred to the Web version of this article.)

different aspects of Fe25 nanowires; at this scale they exhibit a quite irregular and "granular" morphology (Fig. 4a) with mean lengths <1.7 μm. They are composed of very small grains of *fcc* γ-Rh(Fe) phase, as can be observed in the SAED pattern (Fig. 4 a inset) and the HRTEM image in Fig. 4 b, where a grain oriented in the [011] *fcc* zone axis can be identified by its FFT in the inset of the figure. To obtain a statistical analysis of the grain size, bright and dark field images were acquired, as shown in Fig. 4c and d. The wires' diameter distribution in the array and the γ-Rh(Fe) phase grain diameter were also fitted by log-normal functions, leading to a mean nanowire diameter of (10 ± 3) nm and a mean grain size of (4 ± 1) nm (Fig. 4e and 4f). The composition of the small γ-Rh(Fe) grains, obtained from EDS spectra, results in (29 ± 5) at.% Fe - (71 ± 5) at.% Rh (Fig. 4g), which is statistically indistinguishable from the composition of this phase in Fe54 nanowires.

The morphology and structure of Fe15 nanowires are very

similar to the ones of samples Fe25; Fig. 5 resume the main results for these nanowires. From the overview of the nanowires and the corresponding SAED pattern (Fig. 5a), it can be observed that they also exhibit an irregular morphology, are single-phase and composed by γ-Rh(Fe) *fcc* grains. In the HRTEM image shown in Fig. 5 b, even though the small grains cannot be clearly identified, a ring corresponding to the 111 reflection of the *fcc* γ-Rh(Fe) grains can be observed in the FFT of the image. Fig. 5c and 5 d illustrate typical bright and dark field images of the nanowires, from which the histograms in Fig. 5e and 5 f were built; a mean wire diameter of (17 ± 5) nm and a grain size of (2.1 ± 0.9) nm were obtained. The composition of these nanowires was estimated from EDS spectra in (14 ± 3) at.% Fe - (86 ± 3) at.% Rh (Fig. 5g). The very small sizes of the γ-Rh(Fe) phase, observed in the three samples investigated, explained the absence of intense diffraction lines of this phase in the XRD profiles shown in Fig. 2.

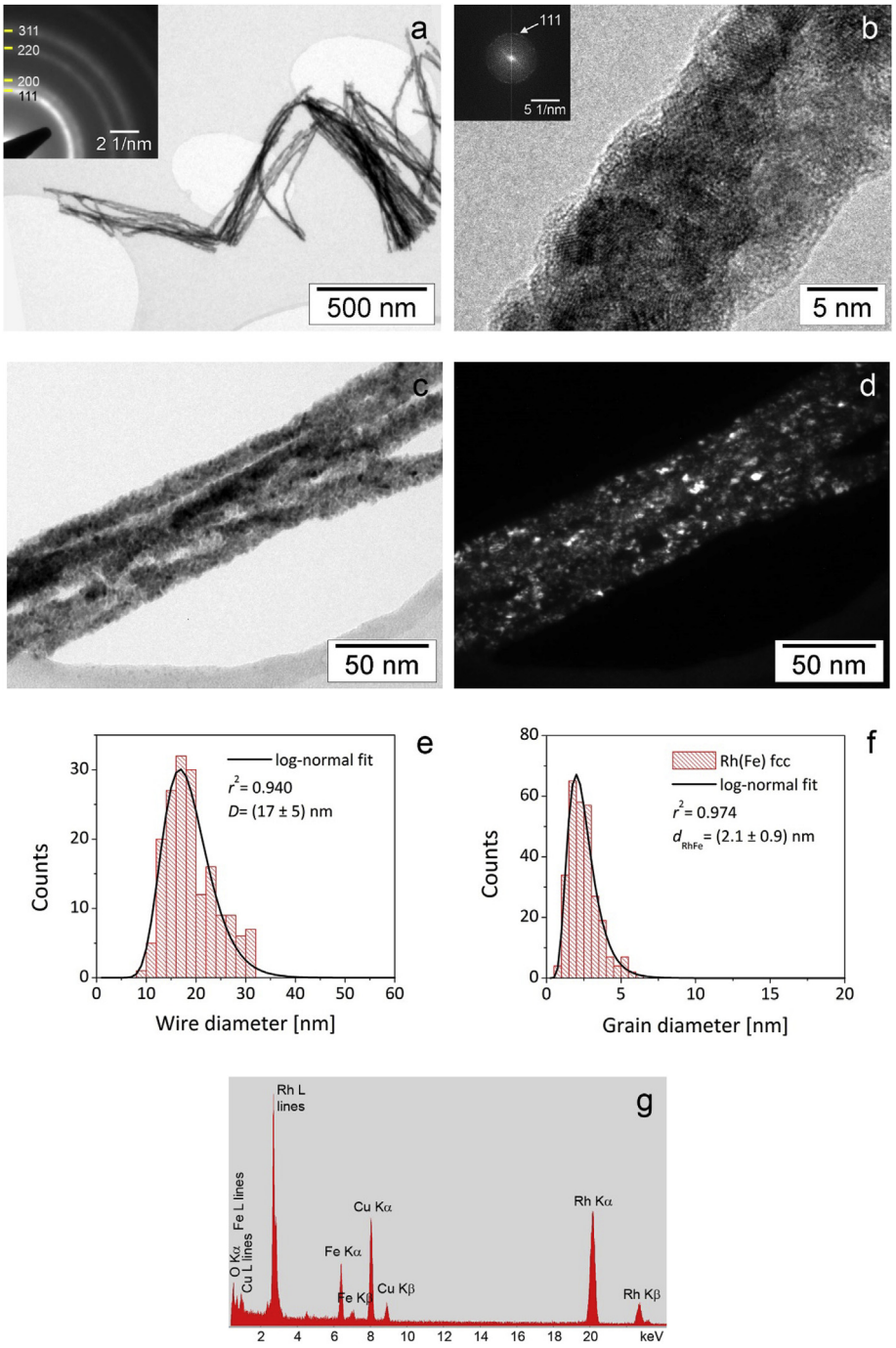

Fig. 5. Fe15 nanowires. (a) TEM overview. The corresponding SAED pattern is included as an inset. Electron diffraction rings of γ-Rh(Fe) *fcc* phase are indicated with yellow segments. (b) HRTEM image of a Fe15 nanowire. The FFT of the complete image shows a ring corresponding to 111 *fcc* reflection. (c) Bright field TEM image of a bunch of Fe15 nanowires and (d) corresponding dark field image with 111 *fcc* reflection. (e) Wire diameter and (f) grain size histograms and corresponding log-normal fits, resulting from TEM data. (g) EDS spectrum of the γ-Rh(Fe) phase nanowires. Cu lines arise from the TEM grid. (For interpretation of the references to colour in this figure legend, the reader is referred to the Web version of this article.)

3.2. Temperature dependence of the hysteresis properties

Magnetic hysteresis loops of Fe54 nanowire arrays are shown in Fig. 6; polarization vs. magnetic field was measured with the field applied parallel (PA) and perpendicular (PE) to the nanowire long axis. Samples are predominantly ferromagnetic in the entire temperature range between 5 K and 300 K as shown in Fig. 6a and 6 b. respectively, mainly due to the large α-Fe grains; they exhibit the magnetization easy axis along the nanowire axis due to a large aspect ratio, leading to appreciable shape anisotropy.

The hysteresis loops corresponding to samples Fe25 are displayed in Fig. 7. In this case the loop at 5 K (below the $T_{sg} = 40$ K) and that at 300 K are also both ferromagnetic-like. It is worth noting that loops Fe25 and Fe15 show a relatively large diamagnetic contribution and that the magnetic signal (about 50–70 μemu) is one magnitude order lower than in Fe54 (about 800 μemu). Nanowires Fe15 also exhibit a ferromagnetic-like behavior at low temperature but above 40 K the loops have a predominant diamagnetic contribution arising from the alumina template as shown in Fig. 8. Only a small kink near zero fields suggests a very small superparamagnetic contribution. The *fcc* γ-Rh(Fe) phase in all the nanowires in the present work have very small grain size (2–4 nm), leading to large volume fractions of the chemically and atomically disordered phase at the grain boundaries. Then the different behaviors of Fe25 and Fe15 nanowires may be explained by a lower Fe content and the smaller grain size in samples Fe15.

Coercivity and squareness measured at 5 K as functions of the iron content in the nanowires are not monotonic, but depend on the phases formed (Fig. 9). Hysteresis is observed at this temperature because all samples undergo collective magnetization mechanisms. Larger values of $\mu_0 H_C$ and S correspond to samples with high iron contents (>50%) because they all contain the *bcc* α-Fe phase, contributing to high values of shape anisotropy. As expected, a lower magnetic hardness is observed in nanowires with less iron content and entirely composed by small ferrimagnetic *fcc* γ-Rh(Fe) grains, exchange coupled through the frozen spin-glass intergranular phase.

Magnetization vs. temperature was measured between 5 K and 300 K for the PA orientation, following the Zero Field Cooling-Field Cooling (ZFC-FC) protocol, under an applied magnetic field of 10 mT. Fig. 10 depicts these curves, which display special features. All the curves show hysteresis: that corresponding to Fe54 displays ferromagnetic-like characteristics above 50 K, with an irreversibility temperature above 300 K. In Fe25 nanowires the temperature of complete irreversibility is also above 300 K, but the curve profile suggests a ferromagnetic-like contribution probably associated to blocked grains [19]. That corresponding to Fe15 is superparamagnetic-like above 50 K. The ferromagnetic behavior of Fe54 in all the temperature range is expected due to the large α-Fe segments present in the wires. However, the bulk γ-Rh(Fe) phase is reported to be paramagnetic above 273 K.

The three curves exhibit a marked maximum at low temperature, at about 40 K. These maxima are found in the zero field cooled sample, in the subsequent cooling under a static field of 10 mT and in the second heating (the actual field cooled curve). A similar behavior has been reported by different authors in bulk Fe-Rh alloys where a highly disordered γ-Rh(Fe) (in metastable or stable condition) is present [20–22]. In fact, they demonstrated that the maxima and also the irreversibility in the curves displayed in Fig. 10 are associated with a nanometric grain size, in particular with a spin-glass-like phase in the intergranular region. The coexistence of both ferromagnetic and antiferromagnetic interactions in Fe-Rh alloys, added to chemical disorder and a broad distribution of interatomic distances in the highly disordered intergranular region, are likely to account for this spin-glass-like phase. In this picture the local temperature maxima at $T_{sg} \cong 40$ K correspond to the spin-glass phase freezing. Then, the different magnetic regimes observed below and above T_{sg}, arise from the spin-glass-like character of this intergranular region.

The behavior exhibited by the (Fe, Rh) containing nanowires are conditioned by the coexistence and significant interplay of ferro- and antiferromagnetic interactions. Navarro et al. [21] propose that nanocrystalline Fe_xRh_{100-x} ($x \leq 50$) alloys consist of an ensemble of weak ferrimagnetic-like nanocrystals or grains, with uncompensated magnetic moment, which are surrounded by an external shell with spin-glass-like characteristics. Considering that in the central part of the grains magnetic disorder is also expected, these grains are more likely to have sperimagnetic order, more than ferrimagnetic as proposed by Ref. [21]. At low temperature, the exchange between uncompensated moments in the nanograins, carried through the frozen moments of the boundaries, gives rise to a cluster glass arrangement and the sample magnetizes cooperatively. As the temperature rises reaching the freezing temperature of the boundary phase, the grains become uncoupled and the susceptibility reaches a maximum. Above this freezing temperature, depending on the grain size and the distribution width, these grains may behave as pararamagnetic, superparamagnetic or as blocked single domains (ferromagnetic like). This is confirmed by

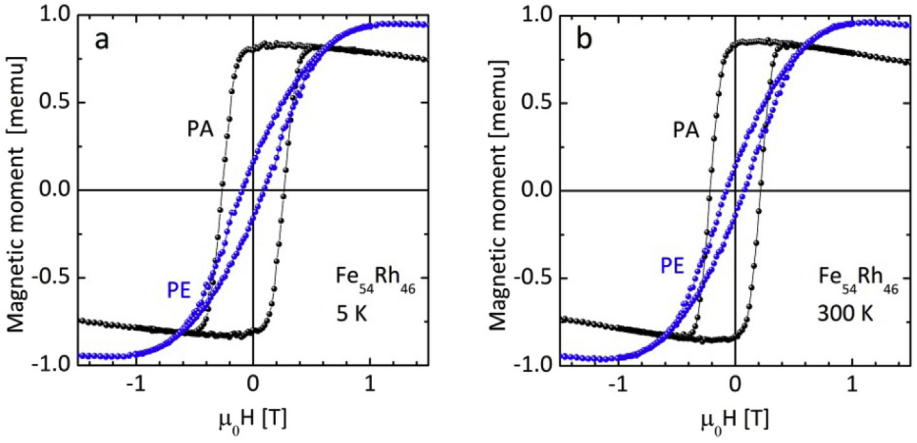

Fig. 6. Magnetic hysteresis loops of Fe54 nanowire arrays. PA and PE indicate that the magnitude is measured with the magnetic field applied parallel or perpendicular to the nanowire major axis at (a) 5 K and (b) 300 K.

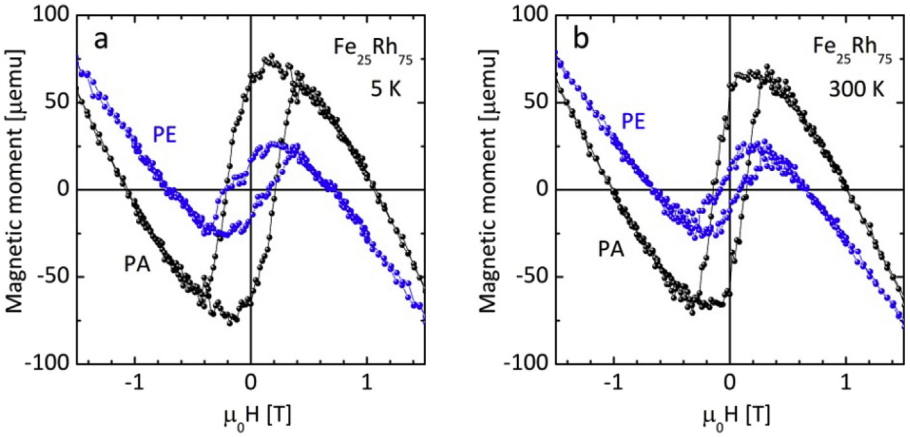

Fig. 7. Magnetic hysteresis loops of Fe25 nanowires. PA and PE indicate that the magnitude is measured with the magnetic field applied parallel or perpendicular to the nanowire major axis at (a) 5 K and (b) 300 K.

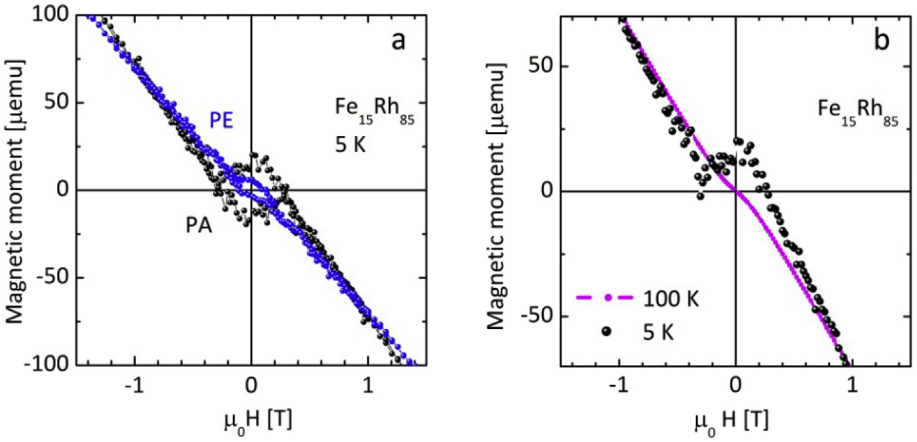

Fig. 8. Magnetic hysteresis loops of Fe15 nanowires (a) at 5 K in PA and PE orientation and (b) upper branch of the hysteresis loop in (a) and at 100 K (smoothed), which is above the spin glass freezing temperature (40 K) measured in the PA orientation.

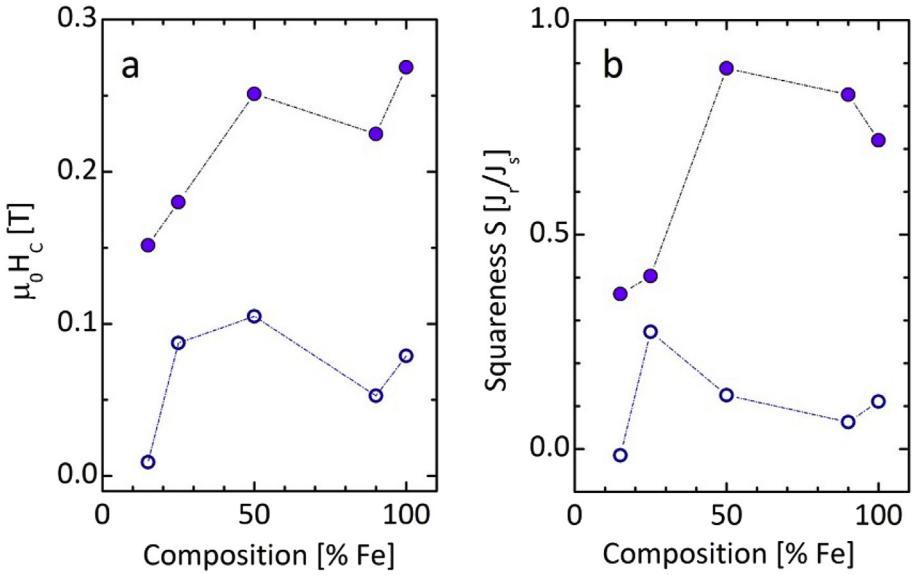

Fig. 9. Coercive field (a) and squareness (b) as a function of the Fe content in nanowires arrays at 5 K, for PA (solid) and PE (open) positions. Data corresponding to Fe and $Fe_{90}Rh_{10}$ are taken from Ref. [12].

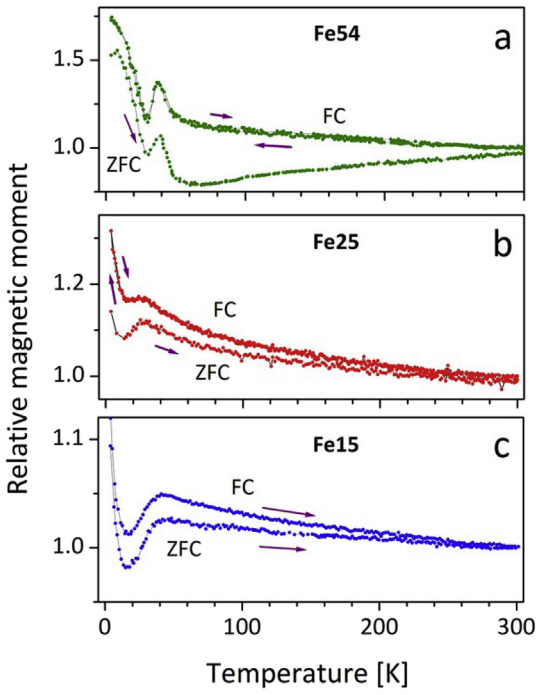

Fig. 10. ZFC-FC polarization curves for (a) Fe54, (b) Fe25 and (c) Fe15 nanowire arrays, measured with an applied field of 10 mT parallel to the nanowire major axis.

Mössbauer Effect Spectroscopy [22] in samples $Fe_{50}Rh_{50}$ and $Fe_{26}Rh_{74}$ obtained by melt-spinning and subsequent intensive ball-milling, with grain sizes of 6–12 nm.

The hysteresis loops of as-prepared nanowire arrays Fe54 and Fe25 were measured at different temperatures between 50 K and 300 K. The evolution of coercivity and squareness with temperature, are shown in Fig. 11. Both magnitudes gradually increase at low temperature; coercivity as well as squareness are larger in samples Fe54, as expected for an effective anisotropy ruled by magnetostatic/shape effects.

Assuming a thermally activated, nucleation controlled magnetization reversal mechanism, the temperature and field dependence of the activation energy barrier and the coercive field may be described as [23]:

$$E = E_0\left(1 - \frac{H}{H_0}\right) \tag{2}$$

$$\mu_0 H_C = \mu_0 H_0 - \left[\frac{\mu_0 H_0 25\, k_B}{E_0}\right] T. \tag{3}$$

Here parameters E_0 and $\mu_0 H_0$ are the apparent activation barrier height and the critical field for reversal, respectively, extrapolated to T = 0 K. The slope is then given by $\beta = \frac{\mu_0 H_0 25\, k_B}{E_0}$. Values for these parameters, determined by a linear fitting of experimental data are given in Table 1, together with values corresponding to Fe nanowires for comparison [13]. The activation energy values are comparable to those reported (2.4–5.1 eV) for a mechanism of inverse domain nucleation in Fe nanowires by Paulus et al. [24].

The apparent activation energy barrier is found to decrease as the Fe content reduces, suggesting that shape anisotropy is important. In the cases of Fe and Fe54 nanowires, nucleation (curling in a critic volume [25]) takes place in the *bcc* α-Fe phase while in Fe25, the nucleus form in the ferrimagnetic *fcc* γ-Rh(Fe) granular phase, still blocked above 40 K up to room temperature.

4. Conclusions

For the first time, Rh-rich Fe-Rh granular nanowires with very small grain size have been synthesized by AC electrodeposition into porous alumina templates, and their magnetic properties evaluated. Near the nominal equiatomic concentration nanowires are biphasic, composed of large α-Fe grains and between them, agglomerates of quite small (~3 nm) grains of γ-Rh(Fe) phase. Nanowires with lower Fe concentrations (Fe25 and Fe15) are single phase, conformed by very small grains of γ-Rh(Fe) phase, with mean sizes of about 2–4 nm. At low temperature, a reversible local maximum is observed in the magnetization vs. temperature curves

Table 1
Parameter values arising from the best fit of eqn. (3) to data shown in Fig. 9 a. Critical switching field at T = 0 K, $\mu_0 H_0$, slope given by $\beta = \frac{\mu_0 H_0 25\, k_B}{E_0}$ and the resulting values of activation energy E_0 are given in eV and in kJ/mol.

Sample	$\mu_0 H_0$ [mT]	β [10^{-4} T/K]	E_0 [eV]	E_0 [kJ/mol]
Fe	253 ± 4	−2.1 ± 0.2	2.6	250
Fe54	166 ± 2	−1.7 ± 0.1	3.1	298
Fe25	75 ± 2	−0.7 ± 0.2	2.3	229

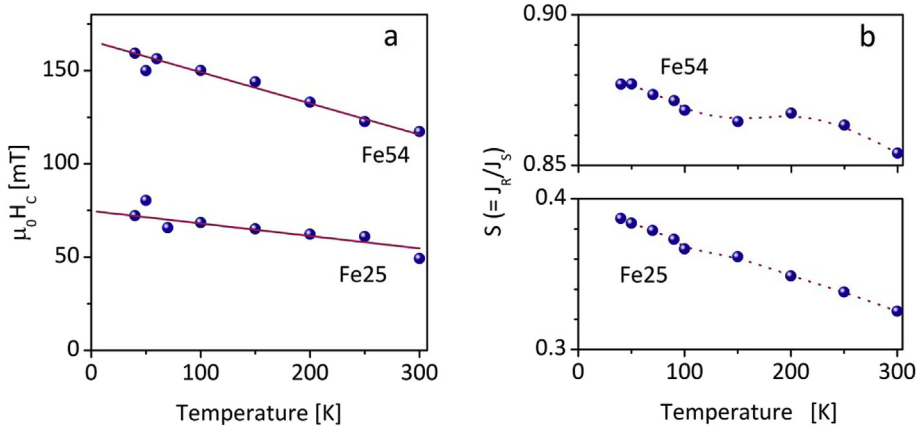

Fig. 11. Coercivity (a) and squareness (b) in Fe54 and Fe25 nanowires measured with the applied field parallel (PA) to the nanowire major axis at different temperatures.

near 40 K in all the samples, which arise from the γ-Rh(Fe) phase. This temperature is consistent with the freezing of a spin-glass-like phase at the grain boundaries of the γ-Rh(Fe) phase. Hysteresis loops measured at 5 K indicate that all samples are ferromagnetic. Above 40 K samples with 54 at.% Fe (Fe54) are also ferromagnetic because of the large α-Fe grains. Samples with 25 at.% Fe (Fe25) behave as ferromagnets due to a blocked superparamagnetic phase composed by ferrimagnetic uncoupled grains. Instead, samples with the lower iron content (Fe15) and the smaller grain size are superparamagnetic from 40 K to 300 K. Below 40 K the Rh-rich samples exhibit a cooperative, ferromagnetic-like behavior, due to the freezing of the grain boundary disordered phase with the consequent exchange coupling of grains through this intergranular phase. Above 40 K, the coercive fields in samples Fe54 and Fe25 are linear functions of temperature, indicating that the magnetization reversal mechanism is controlled by the nucleation of inverse domains.

Acknowledgements

Financial support provided by Secyt-UNC and Conicet, Argentina, is gratefully acknowledged.

References

[1] Y. Xu, L. Chen, X. Wang, W. Yao, Q. Zhang, Recent advances in noble metal based composite nanocatalysts: colloidal synthesis, properties, and catalytic applications, Nanoscale 7 (2015) 10559.
[2] T. Hyeon, Chemical synthesis of magnetic nanoparticles, Chem. Commun. 8 (2003) 927.
[3] K.M. Kang, K.M. Kim, I.W. Shim, H.Y. Kwak, Catalytic test of supported Ni catalysts with core/shell structure for dry reforming of methane, Fuel Process. Technol. 92 (2011) 1236.
[4] R. W, Sibin Duan, Bimetallic nanostructures with magnetic and noble metals and their physicochemical applications, Prog. Nat. Sci.: Materials International 23 (2013) 113.
[5] J.M. Lee, W. Lee, Effects of surface roughness on hydrogen gas sensing properties of single Pd nanowires, J. Nanosci. Nanotechnol. 3 (2011) 2151.
[6] J.B. Mc Kinnon, D. Melville, E.W. Lee, The antiferromagnetic-ferromagnetic transition in iron-rhodium alloys, J. Phys. Chem. Metal Phys. Suppl 1 (1970) S46.
[7] G. Shirane, C.W. Chen, P.A. Flinn, R. Nathans, Mössbauer study of hyperfine fields and isomer shifts in the Fe-Rh alloys, Phys. Rev. 131 (1963) 183.
[8] M.P. Annaorazov, M. Ünal, S.A. Nikitin, A.L. Tyurin, K.A. Asatryan, Magnetocaloric heat-pump cycles based on the AF–F transition in Fe–Rh alloys, J. Magn. Magn. Mater. 251 (1) (2002) 61–73.
[9] M. Manekar, S.B. Roy, Reproducible room temperature giant magnetocaloric effect in Fe–Rh, J. Phys. D Appl. Phys. 41 (2008), 192004.
[10] S. Cai, D. Wang, Z. Niu, Y. Li, Progress in organic reactions catalyzed by bimetallic nanomaterials, Chin. J. Catal. 34 (2013) 1964.
[11] M. Shokouhimehr, Magnetically separable and sustainable nanostructured catalysts for heterogeneous reduction of nitroaromatics, Catalysts 5 (2015) 534.
[12] J.S. Riva, G. Pozo-López, A.M. Condó, M.S. Viqueira, S.E. Urreta, D.R. Cornejo, L.M. Fabietti, Biphasic Fe-Rh nanowires synthesized by AC electrodeposition, J. Alloy. Comp. 688 (2016) 804.
[13] J.S. Riva, G. Pozo-López, A.M. Condó, J.M. Levingston, Luis M. Fabietti, Silvia E. Urreta, Magnetic viscosity in iron-rhodium nanowires, J. Alloy. Comp. 709 (2017) 531.
[14] H. Masuda, K.S. Fakuda, Ordered metal nanohole arrays made by a two-step replication of honeycomb structures of anodic alumina, Science 268 (1995) 1466.
[15] K. Nielsh, J. Choi, K. Schwirn, R.B. Wehrspohn, U. Gosele, Nano Lett. 2 (2002) 677.
[16] M. Stearns, Y. Cheng, Determination of para- and ferromagnetic components of magnetization and magnetoresistance of granular Co/Ag films (invited), J. Appl. Phys. 75 (1994) 6894.
[17] Clinton C. Chao, Pol Duwez, Chang C. Tsuei, Metastable fcc Fe–Rh alloys and the Fe–Rh phase diagram, J. Appl. Phys. 42 (1971) 4282.
[18] L.J. Swartzendruber, ASM Handbook Volume 3: Alloy Phase Diagrams, vol. 3, 1998, p. 853. ISBN 0-87170-381-5.
[19] M. Knobel, W.C. Nunes, L.M. Socolovsky, E. De Biasi, J.M. Vargas, J.C. Denardin, Superparamagnetism and other magnetic features in granular materials: a review on ideal and real systems,, J. Nanosci. Nanotechnol. 8 (2008) 2836.
[20] A.P. Murani, B.R. Coles, Interactions between anomalous local moments: magnetic ordering in rhodium-iron alloys, J. Phys. Chem.: Met. Phys. 2 (1970) S159.
[21] E. Navarro, A. Hernando, A.R. Yavari, D. Fiorani, M. Rosenberg, Grain-boundary magnetic properties of ball-milled nanocrystalline Fex Rh100−x alloys, J. Appl. Phys. 86 (1999) 2166.
[22] G. Filoti, V. Kuncse, E. Navarro, A. Hernando, M. Rosenberg, J. Alloy. Comp. 278 (1998) 60.
[23] J. Vogel, J. Moritz, O. Fruchart, Nucleation of magnetization reversal, from nanoparticles to bulk materials C, R. Physique 7 (2006) 977–987.
[24] P.M. Paulus, F. Luis, M. Kröll, G. Schmid, L.J. de Jongh, Magnetic properties of densely packed arrays of Ni nanowires as a function of their diameter and lattice parameter, J. Magn. Magn Mater. 224 (2001) 180.
[25] M.S. Viqueira, N. Bajales, S.E. Urreta, P.G. Bercoff, Magnetization mechanisms in ordered arrays of polycrystalline Fe100-xCox nanowires, J. Appl. Phys. 117 (2015) 204302.